Check for updates

Chemistry – A European Journal

ChemEurJ Chemistry Europe European Chemical Societies Publishing

RESEARCH ARTICLE OPEN ACCESS

Structure–Activity Relationships in Methyl-Driven Overhauser Effect DNP

Ananya Mukherji[1] | Emma A. Foley[2] | Shubha S. Gunaga[3] | Thierry Dubroca[3] | Mukaila A. Ibrahim[1] | Jin-Seok Yi[1] | Nisreen Sharara[1] | Syed Raza[1] | Fadwat Bazzi[1] | Simona Marincean[1] | Dragos F. Flesariu[4] | Panayiotis A. Koutentis[4] | Frédéric Mentink-Vigier[3,5] | Takeshi Kobayashi[6] | Christos P. Constantinides[1] | Frédéric A. Perras[2,6]

[1]Department of Natural Sciences, University of Michigan-Dearborn, Dearborn, Michigan, USA | [2]Department of Chemistry, Iowa State University, Ames, Iowa, USA | [3]National High Magnetic Field Laboratory, Florida State University, Tallahassee, Florida, USA | [4]Department of Chemistry, University of Cyprus, Nicosia, Cyprus | [5]Department of Chemistry & Biochemistry, Florida State University, Tallahassee, Florida, USA | [6]Chemical and Biological Sciences Division, Ames National Laboratory, Ames, Iowa, USA

Correspondence: Christos P. Constantinides (cconst@umich.edu) | Frédéric A. Perras (fperras@ameslab.gov)

Received: 14 May 2026 | **Revised:** 11 September 2026 | **Accepted:** 23 September 2026

ABSTRACT

Dynamic nuclear polarization (DNP) enables dramatic sensitivity enhancements in solid-state nuclear magnetic resonance studies of materials. Most DNP approaches rely on the cross effect mechanism that typically employs nitroxide biradicals that are chemically incompatible with many samples and whose efficiency decreases with increasing magnetic field strength. The Overhauser effect DNP mechanism is a potential alternative that allows the use of a broader range of radical polarizing agents but requires further development. Mixed-valence and methyl-functionalized conjugated radicals have both been shown to enable Overhauser DNP, yet general design rules remain elusive. Here, we studied a series of 14 methyl-functionalized Blatter-type radicals to elucidate key structure–activity relationships. We found that radicals with sterically unhindered methyl groups are active, a feature readily identifiable from a Kekulé structure. Substitutions that alter molecular conformation, and thus the spin density distribution, predictably reduce performance. Addition of trifluoromethyl groups, commonly employed to enhance stability, also decreases activity by withdrawing spin density from Overhauser-active sites. These findings provide design principles that accelerate the discovery of efficient methyl-driven Overhauser effect DNP polarizing agents.

1 | Introduction

Dynamic nuclear polarization (DNP) is a technique that can dramatically enhance nuclear magnetic resonance (NMR) signal intensities by transferring magnetization from highly-polarized unpaired electron spins to nuclear spins [1–3]. Its commercialization [4, 5] has led to numerous applications in materials science and biology, where the increased sensitivity enables measurements of dilute species, such as complex multicomponent biological systems [6–10], and detection of surface or edge sites in materials [11–19].

To date, DNP applications for structural studies have primarily relied on nitroxide-based polarizing agents [20–22]. Bisnitroxides are highly active in the cross effect (CE) mechanism and can reliably produce enhancement factors (ε) exceeding 100 in most real-world samples. These agents, however, present challenges for materials applications: nitroxides are strong oxidizing agents [23] and can react with or degrade the sites of interest in heterogeneous catalysts [24, 25]. As such, DNP is sometimes avoided in favor of conventional solid-state NMR spectroscopy. Consequently, strategies have been developed to mitigate nitroxide-induced damage, either

This is an open access article under the terms of the Creative Commons Attribution-NonCommercial License, which permits use, distribution and reproduction in any medium, provided the original work is properly cited and is not used for commercial purposes.
© 2026 The Author(s). *Chemistry - A European Journal* published by Wiley-VCH GmbH.

via phase segregation [26–29] or by generating radicals in situ [30–33].

An alternative approach is to employ non-nitroxide radicals as polarizing agents [34–40]. Carbon-centered and conjugated radicals, however, generally lack sufficient *g*-tensor anisotropy to mediate CE DNP for ^{1}H spins [41, 42] and are therefore primarily active in the solid effect (SE) mechanism. SE involves formally forbidden electron-nuclear zero- or double-quantum transitions and is less efficient than CE [43]. Another mechanism, the Overhauser effect (OE) [1, 2], can be active in some monoradicals and requires only saturation of the fundamental, allowed electron paramagnetic resonance (EPR) transition [44]. OE arises from cross-relaxation driven by modulation of electron-nuclear couplings in the presence of electron or molecular motions and has been observed in conductive molecules [45], metals [2, 46], liquids [47, 48], mixed-valence radicals [34, 49–53], and conjugated radicals bearing rapidly rotating methyl groups [37, 54–56]. Unlike SE, OE has the potential to achieve high efficiency at typical NMR magnetic fields [49, 57], but the molecular motions driving the effect must be optimized, similar to the work on bisnitroxide CE polarizing agents from the previous two decades [21, 22, 58–64].

This work focuses on methyl-driven OE DNP in conjugated radicals possessing methyl substituents [37, 55, 56]. We synthesized an array of 14 Blatter-type [65] radicals bearing one to three methyl groups. These radicals probe the relevant chemical space in the Blatter system with the goal of identifying trends that correlate the OE activity and structural features. Mechanistic insights are combined with quantum chemical investigations, which were recently demonstrated to correlate well with experimental DNP measurements [56].

2 | Experimental Section

2.1 | Synthesis

The Blatter radicals described here were prepared using a post-cyclization organolithium addition strategy related to our previously reported method for access to 1,4-dihydrobenzo[*e*][1,2,4]triazin-4-yl radicals [66]. In this approach, the appropriate aryllithium reagent is added to the benzo[*e*][1,2,4]triazine precursor [66–70] to give an intermediate anion, which upon exposure to air is oxidized to the corresponding radical. This strategy enables post-cyclization introduction of the N(1) aryl substituent onto preformed benzotriazine precursors to afford Blatter radicals, bypassing amidrazone-based routes that can involve oxidatively sensitive intermediates. Additional details are given in the supporting information. Radicals **3** and **7** were prepared according to literature procedures [71, 72]. The EPR spectra of the radicals are given in Figures S1–S12.

2.2 | Single-Crystal X-Ray Diffraction

Single-crystal x-ray diffraction data were collected on a Rigaku XtaLAB Synergy Dualflex diffractometer equipped with a HyPix-Arc 150 detector using Cu K_α radiation (λ = 1.54184 Å). The crystals were maintained at *ca*. 100 K during data collection. Unit-cell refinement, data reduction, scaling, and absorption corrections were performed using *CrysAlisPro* 1.171.44.118a [73]. Absorption corrections were applied using numerical Gaussian integration over a multifaceted crystal model and empirical correction using spherical harmonics, as implemented in the SCALE3 ABSPACK scaling algorithm [73]. The structures were solved and refined using Olex2 1.5-alpha as the graphical interface [74], with *SHELXT 2018/2* used for structure solution by dual methods [75] and *SHELXL 2019/3* used for full-matrix least-squares refinement on F^2 [76]. All non-hydrogen atoms were refined anisotropically, and hydrogen atoms were placed in calculated positions and refined using the riding model. Deposition numbers 2546239 (for **1p**), 2546240 (for **6**), 2546241 (for **1o**), 2546242 (for **1o,6CF$_3$**), 2546243 (for **1op,6CF$_3$**), and 2546244 (for **5**) contain the supplementary crystallographic data for this paper. These data are provided free of charge by the joint Cambridge Crystallographic Data Centre and Fachinformationszentrum Karlsruhe Access Structures service. Crystallographic data are also summarized in Tables S1–S38.

2.3 | Dynamic Nuclear Polarization

Most DNP experiments were performed using a Bruker AVANCE III 400 magic-angle spinning (MAS)-DNP spectrometer equipped with a 3.2 mm low-temperature MAS probe at 100 K. Radicals were dissolved in 1,1,2,2-tetrachloroethane (TCE) at a concentration of 40 mM and used immediately. Solutions were injected into 3.2 mm sapphire rotors that were then inserted into the pre-cooled probe. Samples were then degassed by ejecting the rotor, leaving it to thaw under nitrogen flow for 10 seconds in the sample catcher, and reinserting it into the cold probe twice before spinning the rotor to a final frequency of 10 kHz. DNP build-up times (T_{DNP}) were measured with the use of a saturation recovery experiment using a 2.5 µs excitation pulse. DNP field sweep profiles were acquired in real time during the magnetic field sweep using a short (1 µs) low tip angle excitation pulse. Identical sweeps were performed with and without the application of microwaves to determine the frequency-dependent DNP enhancement factors (ε). To minimize offset issues, sweeps were performed in halves (frequencies above or below the OE maximum).

The OE DNP enhancements were also measured at a higher magnetic field strength of 14.1 T using a Bruker AVANCE NEO 600 MHz MAS-DNP NMR spectrometer. The sample preparation followed the procedure described above. DNP enhancements were measured with the use of ^{1}H Hahn echo measurements and confirmed with the use of one-dimensional ^{1}H-^{13}C cross-polarization spectra.

2.4 | Solid State Electron Paramagnetic Resonance

EPR experiments were conducted at W-band (94 GHz, 3.4 T) to obtain the transverse (T_{2e}) and longitudinal (T_{1e}) relaxation times of the Blatter radicals at 100 K to help identify the parameters that control the DNP efficiency. The EPR measurements were performed using the HiPER spectrometer at the National High Magnetic Field Laboratory (NHMFL) in Tallahassee, Florida, USA. HiPER is a high-power pulsed EPR spectrometer, based on the original development at the University of Saint Andrews [77].

15213765, 0, Downloaded from https://chemistry-europe.onlinelibrary.wiley.com/doi/10.1002/chem.71772 by Florida State University, Wiley Online Library on [02/11/2026]. See the Terms and Conditions (https://onlinelibrary.wiley.com/terms-and-conditions) on Wiley Online Library for rules of use; OA articles are governed by the applicable Creative Commons License

Samples were prepared similarly to the ones used for MAS-DNP as explained above. The only difference is in the degassing, which was done by using TCE stored for weeks in a fluorinated ethylene propylene (FEP) vial within a glovebox. This storage technique allows the oxygen gas to diffuse out of the solvent over a few days. Additionally, three rapid freeze/thaw cycles were performed with each sample prior to insertion into the spectrometer to complete the degassing and obtain a good glass, enabling random dispersion and orientation of the radicals within the matrix. T_2 values were measured with the use of a Hahn echo experiment by varying the delay between the excitation and refocusing pulses. T_1 values were again measured using a Hahn echo pulse sequence, albeit with the addition of a pre-saturation pulse. The delay between the pre-saturation pulse and the Hahn echo sequence was varied to measure T_1. Typical pulse lengths of 20 ns and peak power of 400 W were used unless otherwise noted.

2.5 | Density Functional Theory

Density functional theory (DFT) calculations were carried out to calculate the dependence of the hyperfine coupling tensors and relative energy on the methyl rotor phase. All calculations were performed at the PBE/TZP level of theory [78, 79] using the Amsterdam density functional (ADF) program [80]. Potential energy surface scans were performed as a function of the methyl phase in 10° increments, and hyperfine coupling tensor calculations were performed at each increment using ADF's CPL module [81].

3 | Theory

Overhauser DNP enhancement is caused by electron-nuclear cross-relaxation. For cross-relaxation to hyperpolarize nuclear spins, it is required that the hyperfine coupling between these spins be modulated by either molecular motion or electron conduction, and that the electron spin be taken out of equilibrium, typically via the saturation of its EPR line with high-power microwaves.

OEs have been observed in metals and other systems with itinerant electrons, where fluctuations of the electron spin density give rise to time-dependent hyperfine interactions, as well as in liquids, where molecular rotational and translational motions modulate electron-nuclear couplings in an analogous manner [45–48]. It has also been observed in a handful of so-called mixed-valence radicals where intramolecular electron transfer is coupled to molecular vibrational modes [49–53]. Lastly, the effect has been observed with conjugated radicals functionalized with either methyl or trifluoromethyl groups, where the rotation of the substituent modulates the hyperfine coupling by rotating ^{1}H or ^{19}F nuclei in and out of the π network of the singly-occupied molecular orbital (SOMO) [37, 54–56].

Alternative theories have been proposed to explain the effect using a thermal mixing mechanism [82]; however, these do not readily account for all of the observations in the methyl-driven case studied here [44]. Specifically, the deuteration of the methyl group quenches the ^{1}H OE maximum, does not influence the SE enhancements, and leads to the emergence of a ^{2}H OE [37]. This supports a specific role for the methyl protons in the polarization process. The SE mechanism can instead leverage the other protons on the molecule, which all have similar hyperfine interaction strengths [37]. TM would be able to proceed through the other, more numerous protons on the radical and should thus behave similarly upon deuteration as the SE mechanism. Additionally, thermal mixing conditions are expected to lead to a cross-talk between ^{1}H and ^{2}H spin reservoirs [83, 84]. This is not observed under our conditions, given that the differential activity toward ^{1}H and ^{2}H OE DNP of the two variants implies uncoupled reservoirs. In other words, the ^{1}H and ^{2}H spin temperatures are very different. This interpretation is further supported by the fact that simplistic OE models have been shown to reproduce trends in methyl-driven OE DNP [56] as well as other works which suggest a breakdown of TM at temperatures above 5 K [85]. Finally, the characteristic feature persists at a radical concentration of 3 mM (Figure S13), further suggesting a monoradical mechanism.

The zero- and double-quantum relaxation rates, W_0 and W_2, are given by Equations (1) and (2), respectively [86, 87]:

$$W_0 = \frac{1}{10}\left\langle A^2_{\text{aniso}}\right\rangle J(\omega_e - \omega_n) + \frac{1}{2}\left\langle A^2_{\text{iso}}\right\rangle J(\omega_e - \omega_n) \approx \frac{1}{10}\left\langle A^2_{\text{aniso}}\right\rangle J(\omega_e) + \frac{1}{2}\left\langle A^2_{\text{iso}}\right\rangle J(\omega_e) \quad (1)$$

$$W_2 = \frac{3}{5}\left\langle A^2_{\text{aniso}}\right\rangle J(\omega_e + \omega_n) \approx \frac{3}{5}\left\langle A^2_{\text{aniso}}\right\rangle J(\omega_e) \quad (2)$$

The cross-relaxation rate, $R_{\text{e,n}}$, defined as $W_2 - W_0$, may then be expressed as Equation (3), where $\langle A^2_{\text{aniso}}\rangle$ and $\langle A^2_{\text{iso}}\rangle$ represent the squared modulation amplitudes of the anisotropic and isotropic contributions to the hyperfine coupling, and $J(\omega_e)$ refers to the spectral density at the radical EPR frequency (ω_e).

$$R_{\text{e,n}} = W_2 - W_0 \approx \frac{1}{2}\left(\left\langle A^2_{\text{aniso}}\right\rangle - \left\langle A^2_{\text{iso}}\right\rangle\right) J(\omega_e) \quad (3)$$

The anisotropic coupling constant, A_{aniso}, is often dipolar in nature, in which case it may be approximated by Equation (4).

$$A_{\text{aniso}} \approx \left(\frac{\mu_0}{4\pi}\right)\frac{g\mu_B\gamma}{r^3} \quad (4)$$

where μ_0 is the permeability of free space, μ_B is the Bohr magneton, g is the electron g value, γ is the nuclear gyromagnetic ratio, and r is the electron-nuclear distance.

Note that dipolar-based and isotropic cross-relaxation mechanisms have opposite signs. As a result, dipolar-based cross-relaxation leads to negative OE DNP enhancements (ε_{OE}), which are commonly seen in metals and liquids, whereas through-bond coupling leads to positive DNP enhancements. Such positive enhancements are typical of cross-relaxation caused by intramolecular motions, such as in mixed-valence radicals and the methyl-driven OE [44]. In these cases, good agreement between theory and experiment has been obtained when considering exclusively the isotropic contribution [50, 56]. As a result, we expect the following correlation shown in Equation (5) to hold.

$$\varepsilon_{\text{OE}} \propto -R_{\text{e,n}} \approx \frac{1}{2}\left\langle A^2_{\text{iso}}\right\rangle J(\omega_e) \quad (5)$$

15213765, 0, Downloaded from https://chemistry-europe.onlinelibrary.wiley.com/doi/10.1002/chem.71772 by Florida State University, Wiley Online Library on [02/11/2026]. See the Terms and Conditions (https://onlinelibrary.wiley.com/terms-and-conditions) on Wiley Online Library for rules of use; OA articles are governed by the applicable Creative Commons License

The spectral density function, $J(\omega)$, is typically expressed as a Lorentzian. If all motions arise due to a single correlation time τ_c, then it is represented by the expression in Equation (6).

$$J(\omega) = \frac{\tau_c}{1 + \omega^2 {\tau_c}^2} \tag{6}$$

Focusing on methyl-driven OEs, we can assume that the potential energy surface features three potential energy minima as a function of the methyl rotor phase (X-Y-C-H dihedral angle). We can thus simplify the rotation of the methyl group using jump dynamics, where the hyperfine coupling strength is modulated between the A_{iso} values in each of the three potential energy minima ($A_{iso,\,k}$). In Equation (7), $A_{iso,\,max}$ is the largest value of A_{iso} felt by a methyl ^{1}H spin during rotation [55].

$$\left\langle A_{iso}^2 \right\rangle = \left(A_{iso,max} - \frac{\sum_k A_{iso,k}}{3} \right)^2 \tag{7}$$

The correlation time of the rotation can also be estimated at arbitrary temperatures, assuming that the entropy of activation for rotation is negligible, using the Eyring equation (Equation 8), thus enabling the ab initio estimation of $R_{e,n}$ using quantum chemical methods.

$$\tau_c = \frac{h}{k_B T} \exp\left(\frac{\Delta E}{RT}\right) \tag{8}$$

At a temperature (T) of 100 K and a magnetic field strength of 9.4 T, the methyl group is expected to rotate on average at 264 GHz, the EPR frequency, when the rotation barrier (ΔE) is equal to 1.7 kJ·mol^{-1}, thus maximizing $J(\omega_e)$. Large $J(\omega_e)$ values are predicted at lower ΔE values as well, but barriers greater than 5 kJ·mol^{-1} lead to considerably longer correlation times and are expected to be far less efficient for methyl-driven Overhauser DNP, at least when considering only rotation. Methyl librations may also be effective at driving cross-relaxation at low temperatures [55].

It thus follows that for methyl-driven Overhauser DNP to be effective, a methyl rotation barrier of less than 3 kJ·mol^{-1} is required from a methyl situated on a conjugated radical at the site with significant spin density, where we expect A_{iso} to be large. The SOMO must also be in a π system so that there is a high modulation of A_{iso} from 0 to several MHz as the proton spins are rotated in and out of the lobes of the SOMO. A large unmodulated A_{iso}, as is seen in nitroxide radicals, for instance, would not lead to cross-relaxation.

Hyperpolarization is generated on the ^{1}H spins of the methyl (or ^{19}F spins of a CF_3) and must then be distributed to the bulk for detection. This is achieved by nuclear spin diffusion. Spin diffusion is nevertheless impeded by large frequency shifts away from the nuclear Larmor frequency, such as those induce by the mean isotropic hyperfine coupling, $\overline{A_{iso}}$. As a result of this, in ^{19}F Overhauser DNP, radicals with larger ^{19}F $\overline{A_{iso}}$ values generally had slower DNP build-up rates (T_{DNP}) and lower SE enhancements [56]. Thus, at least for ^{1}H spins, spin diffusion is initially accelerated by intramolecular transfer to ^{1}H nuclei with $\overline{A_{iso}}$ values close to zero before being sent into the bulk through intermolecular spin diffusion [88]. These effects are difficult to predict ab initio and contribute to a loss in accuracy in computations of the OE DNP efficiencies of some radicals.

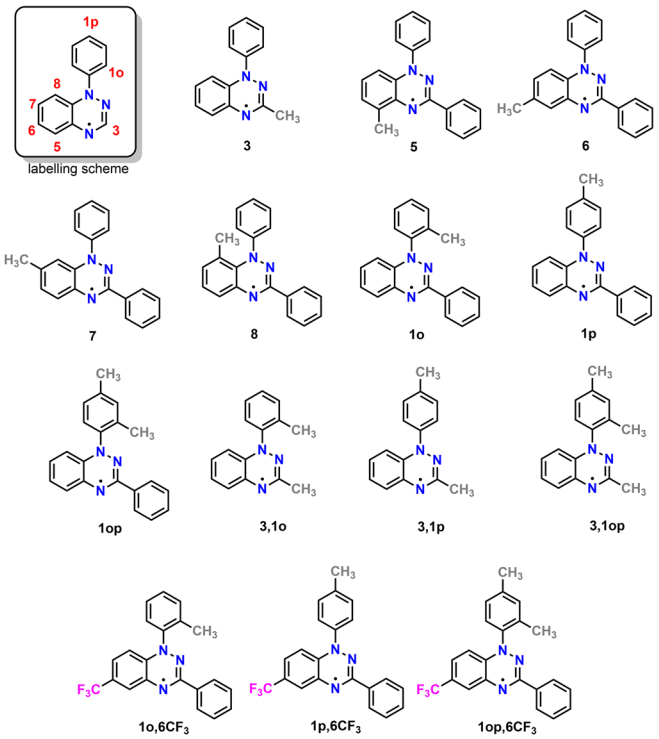


FIGURE 1 | Structures of the CH_3-functionalized radicals studied herein. The radicals are labeled using the site numbering scheme on the top left, where 1o and 1p refer to *ortho* and *para* methyl substitutions on the phenyl moiety located at nitrogen position 1.

4 | Results

The Blatter radical core is depicted on the top left of Figure 1 together with the typical numbering of the 1,2,4-benzotriazine core sites. There is significant spin density throughout this core in addition to the phenyl substituent often placed at the '1' position [89, 90]. We would thus expect a reasonable chance of obtaining OE DNP-active radicals if methyl groups were added to any of the available functionalization sites (positions 3, 5, 6, 7, 8, on the annulated benzene ring and positions *ortho* and *para* on the N1-phenyl moiety). We synthesized each of these possible substituted Blatter radicals to probe chemical trends in DNP activity. In addition to these, multi-functionalized radicals were also prepared with either multiple CH_3 groups or a combination of CH_3 and CF_3 groups. The full list of the radicals is displayed in Figure 1. The radicals are numbered according to the methylated positions; see Figure 1 for reference.

4.1 | Single Crystal Diffraction

Good quality single crystals were obtained for six of the radicals described in this work, which allowed for the investigation of the conformational changes induced by the functionalization. For instance, one may expect the dihedral angle between the 1-aryl group and the benzotriazine core of the radical (φ_{CNCC}) to be of

15213765, 0, Downloaded from https://chemistry-europe.onlinelibrary.wiley.com/doi/10.1002/chem.71772 by Florida State University, Wiley Online Library on [02/11/2026]. See the Terms and Conditions (https://onlinelibrary.wiley.com/terms-and-conditions) on Wiley Online Library for rules of use; OA articles are governed by the applicable Creative Commons License

TABLE 1 | 1-Aryl dihedral angles from single-crystal diffraction.

Radical	φ_{CNCC} / °
Blatter's radical (non-functionalized)	57.90
1o	73.56, 69.50, 73.57, 81.74
1p	35.48
5	45.60, 54.97, 61.26, 46.22
6	42.77
1o,6CF3	78.75
1op,6CF3	60.38

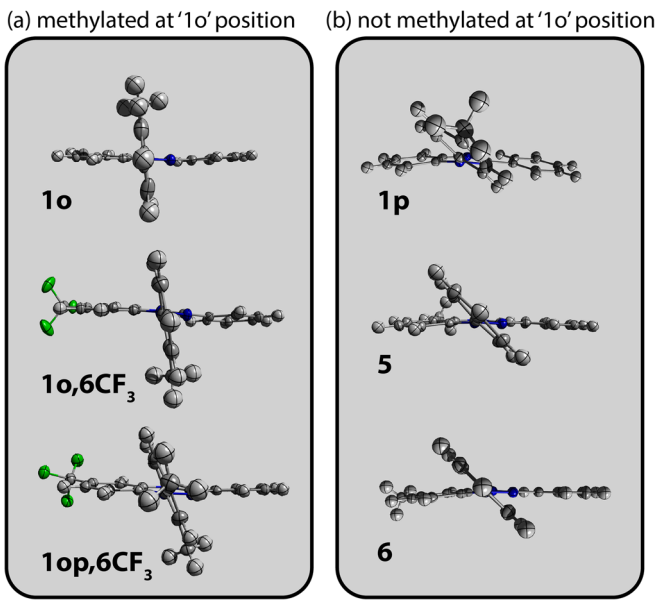


FIGURE 2 | Molecular structures of six methyl-containing Blatter-type radicals viewed down the aryl-N1 bond. They are organized into those that have a methyl at the "1o" position (a) and those that do not (b) to highlight differences in the conformations.

relevance for OE DNP as this dihedral is directly linked to the conjugation of the singly occupied molecular orbital.

We were interested to see whether methyl functionalization at the "1" position led to substantial changes in φ_{CNCC}. Together with the previously published structure of Blatter's radical [91], a total of four structures lacking a methyl group at the "1o" position are available, and three structures with such a functionalization. Their φ_{CNCC} values are summarized in Table 1. Averaged per compound, there is indeed a stark difference between the conformations of the two groups of radicals, with those lacking the functionalization having φ_{CNCC} values of 49 ± 8°, whereas those possessing a methyl group at the "1o" position have a far larger dihedral angle of 73 ± 7°. Molecular structures extracted from the crystal structures are further shown in Figure 2 to highlight this difference. Given that the extent of π conjugation between the two aromatic systems is expected to be roughly proportional to the squared cosine of this angle, we may expect a reduction of the spin density on the 1-aryl moiety by a factor of $\cos^2(49°)/\cos^2(73°) = 5.0$ following the addition of a methyl group at the "1o" position.

4.2 | Singly-Methylated Blatter Radicals

The seven singly-methylated radicals (**1o**, **1p**, **3**, **5**, **6**, **7**, and **8**) allow for the performance of individual methyl locations to be assessed. Cross-relaxation effects are additive [56], and as such, in the absence of correlated effects, polymethylated Blatter radicals should function as the sum of these contributions.

The DNP field sweep profiles of these radicals depicted in Figure 3 enable the differentiation of the active mechanisms for a given radical and the measurement of enhancement factors. The SE mechanism will lead to positive and negative enhancement profiles matching the EPR lineshape, shifted by the addition and subtraction of the nuclear Larmor frequency, respectively. These features are easily differentiated from the OE contribution, which appears as a broad maximum centered on the EPR frequency. To estimate the individual SE, OE, and CE (if discernible) enhancements, we adopted a simulation strategy similar to the one described by Shimon and coworkers [92]. Owing to the more complete saturation of the fundamental EPR lineshape, leading to deviation from a *g* anisotropy lineshape, the OE lineshape was replaced by a Gaussian, and the reported enhancements are those from the largest enhancement observed for the mechanism.

There is clearly a wide range of activities among these radicals. Notably, only four of the seven radicals mediate the OE mechanism, specifically radicals **1p**, **3**, **6**, and **7**, whereas radicals **1o**, **5**, and **8** only display SE and CE features, with a slight positive intensity near the center on radical **5** hinting at possible weak OE DNP. Among the active radicals, a wide range of enhancement factors (ε) from 7 to 21 was observed, suggesting that no single system is yet ideal for OE DNP at 9.4 T and 100 K. The results are summarized in Table 2.

4.3 | Blatter Radicals With Multiple Methyl Groups

In addition to the monomethylated Blatter radicals, we further synthesized four di- or trimethylated variants with permutations of methyl groups at the "1o," "1p," and "3" positions (Figure 1). Their DNP field sweep profiles are shown in Figure 4.

The first observation, comparing the DNP field sweep profiles in red in Figure 4 for radicals **1p**, **3**, and **3**,**1p**, is that the OE enhancements driven by the methyl groups at positions "1p" and "3" are additive. Specifically, OE enhancement factors of 7 and 10 were measured for radicals **1p** and **3,** whereas an OE enhancement factor of 17 was measured for radical **3**,**1p**, which combines both groups. This observation supports the earlier claim we made that the synthesis of conjugated radicals with multiple methyl groups is a promising approach to promoting efficient OE DNP.

The second observation, depicted in each of the overlays in Figure 4, is that the addition of a methyl group to the "1o" position generally leads to a large reduction, or complete quenching, of the Overhauser mechanism.

15213765, 0, Downloaded from https://chemistry-europe.onlinelibrary.wiley.com/doi/10.1002/chem.71772 by Florida State University, Wiley Online Library on [02/11/2026]. See the Terms and Conditions (https://onlinelibrary.wiley.com/terms-and-conditions) on Wiley Online Library for rules of use; OA articles are governed by the applicable Creative Commons License

TABLE 2 | Experimental and computed characteristics of each radical.

Radical	T_{DNP} / s	T_{1e} / µs	T_{2e} / ns	s[a] / µs^2	ε_{OE}[b,c]	site[d]	ΔE / kJ·mol^{-1}	$\overline{A_{iso}}$ / MHz	$\langle A_{iso}^2 \rangle$ / MHz^2	$-R_{e,n}$ / s^{-1}
1o	6.3	649	402	261	0.0 (0.7)	**1o**	3.57	0.26	0.27	0.16
1p	30	207	458	95	7.0 ± 0.5 (3.2)	**1p**	0.16	4.77	24.17	20.50
3	8.3	153	412	63	10.0 ± 0.5 (1.5)	**3**	1.84	−3.26	6.81	19.10
5	12	852	876	746	1.5 ± 0.5 (1.5)	**5**	3.32	3.69	12.70	10.32
6	5.5	685	343	235	16 ± 2 (3.1)	**6**	0.09	3.64	17.40	19.37
7	7.0	580[e]	800[e]	464	21 ± 1 (6.1)	**7**	0.43	7.03	57.44	66.76
8	7.6	532	938	499	1.0 (1.0)	**8**	6.30	−0.05	0.26	0.01
1op	6.5	1940	642	1245	1.0 ± 0.5	**1o**	3.55	0.31	0.29	0.18
						1p	0.09	1.03	1.07	0.84
						total				1.02
3,1o	31	197	257	51	2.0 ± 0.5	**1o**	3.77	0.37	0.46	0.22
						3	1.90	−3.30	5.35	14.83
						total				15.06
3,1p	3.4	299	156	47	17 ± 1	**1p**	0.14	3.96	8.22	12.89
						3	1.83	−3.17	6.55	18.46
						total				31.35
3,1op	38	250	346	87	4.5 ± 0.5	**1o**	3.65	0.26	0.15	0.08
						1p	1.18	1.18	1.43	1.14
						3	1.87	−3.25	5.11	14.25
						total				15.27
1o,6CF$_3$	50	860	269	231	0.0 ± 0.3	**1o**	3.37	0.16	0.02	0.12
						^{19}F	0.44	7.80	113.59	131.93
1p,6CF$_3$	91	880	384	338	6.0 ± 0.6	**1p**	0.12	3.28	11.14	9.06
						^{19}F	0.59	6.04	124.78	172.02
1op,6CF$_3$	50	844	2426	2047	1.0	**1o**	3.33	0.10	0.09	0.07
						1p	0.10	0.58	0.35	0.28
						total	0.42	7.07	139.09	0.35
						^{19}F				158.56

[a]The saturation factor, defined as $s = T_{1e}T_{2e}$.
[b]Values in the parentheses were measured at 395 GHz as opposed to 264 GHz.
[c]When possible, uncertainties were estimated from the goodness of fit of the field sweep profile.
[d]For radicals that contain multiple CH_3 moieties, their rotational and hyperfine characteristics are given separately; the total cross-relaxation rate is the sum of the rates from each group. Note that ^{19}F and ^{1}H cross-relaxation rates do not add.
[e]From reference 55.

To verify that the differences observed are not caused by differences in electron relaxation times, we performed high-field (W-band; 94 GHz; 3.35 T) EPR measurements of the radical solutions to measure their longitudinal (T_{1e}) and transverse (T_{2e}) relaxation times, the product of which relates to the saturation factor. No correlation between the Overhauser DNP enhancements and the saturation factor was observed. Generally, the addition of a methyl group to the '1o' position led to a larger saturation factor despite the lower enhancements (Table 2).

4.4 | Radicals Containing a Trifluoromethyl Moiety

Blatter radicals are electron-rich and are thus stabilized with the addition of electron-withdrawing groups such as trifluoromethyl groups [89]. The addition of such groups could help stabilize polymethylated radicals for OE DNP. It is nevertheless important to determine whether the addition of such groups affects DNP performance. To this aim, we prepared three additional radicals that include a CF_3 group at position "6" (see Figure 1). The DNP field sweep profiles measured for these radicals are depicted in Figure 5, where the profiles from the analogues that exclude this CF_3 are shown in red, with those from the CF_3-containing radicals overlaid in blue.

First, a consistent decrease in SE DNP performance is observed. A similar trend was previously noted when comparing the parent Blatter and radical **7**, where it was attributed to the loss of a key ^{1}H spin with a large static hyperfine coupling, critical for SE DNP [37]. A reduction in OE DNP performance is also observed for radical **1p**, with ε_{OE} decreasing from 6.5 in **1p** to 6.0 in **1p**,**6CF$_3$**.

15213765, 0, Downloaded from https://chemistry-europe.onlinelibrary.wiley.com/doi/10.1002/chem.71772 by Florida State University, Wiley Online Library on [02/11/2026]. See the Terms and Conditions (https://onlinelibrary.wiley.com/terms-and-conditions) on Wiley Online Library for rules of use; OA articles are governed by the applicable Creative Commons License

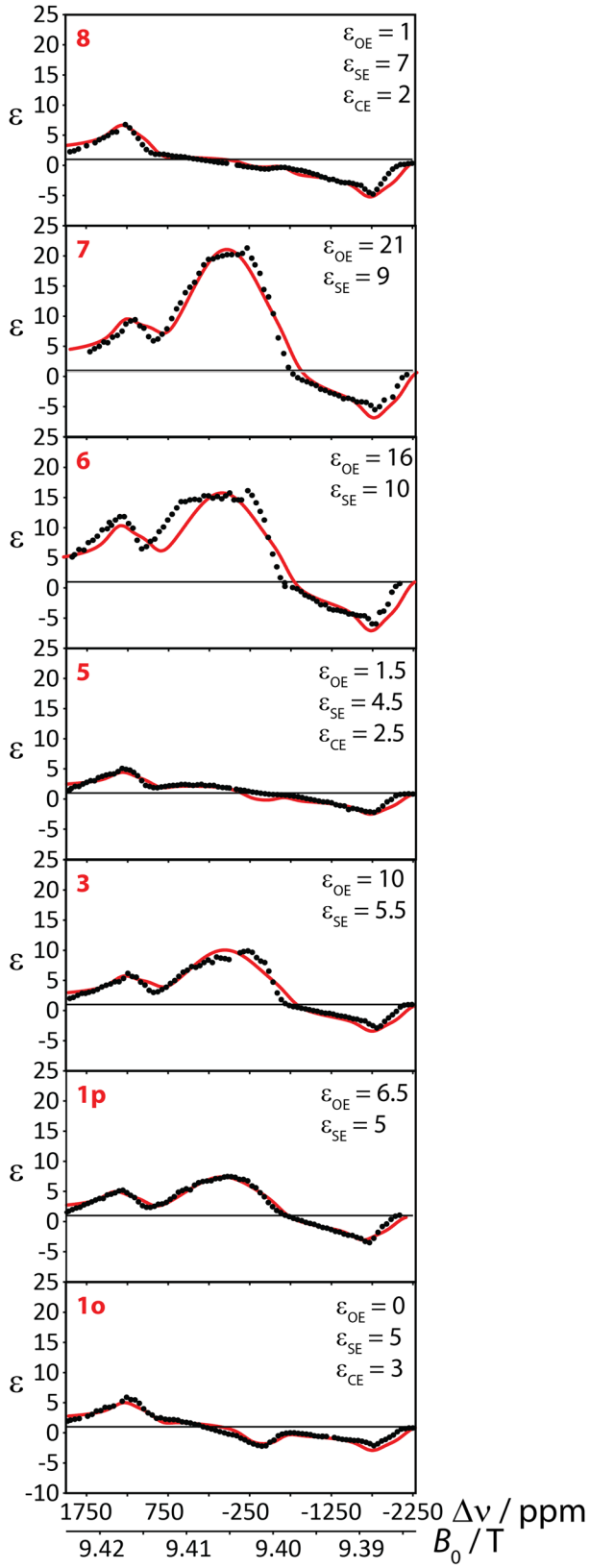


FIGURE 3 | ^{1}H DNP field sweep profiles measured for mono-CH_3-substituted Blatter radicals. Estimates of the DNP enhancements from the different mechanisms are given on the top right of each plot.

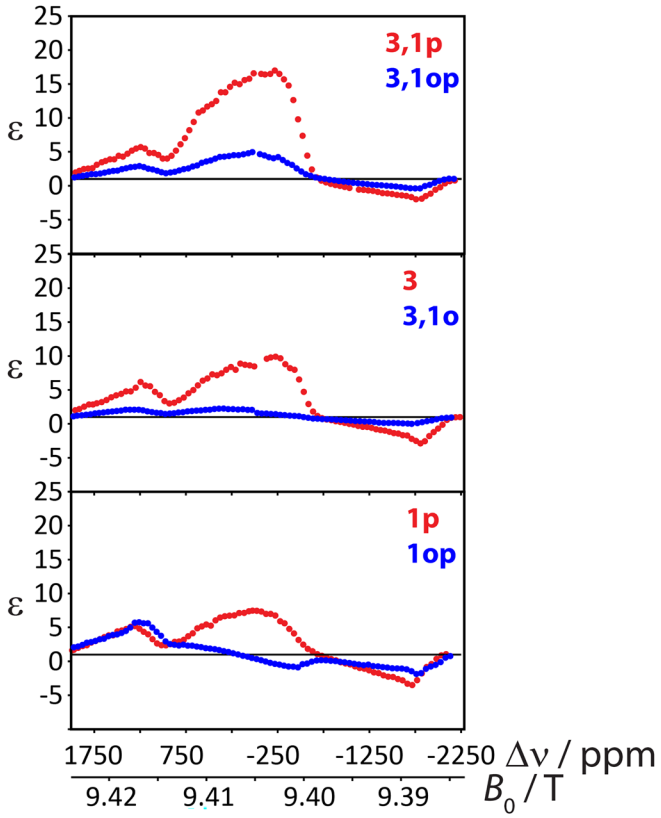


FIGURE 4 | ^{1}H DNP field sweep profiles measured for di- or tri-CH_3-substituted Blatter radicals. Each plot displays an overlay of the DNP field sweep profiles from two radicals that are related by the addition of a methyl group at the 1o position (blue with and red without this methyl). In all cases, a large decrease in efficiency is seen with this addition.

This decrease is modest, suggesting that CF_3 substitution is not strongly detrimental to methyl-driven OE efficiency.

We also probed the efficiency of these radicals in mediating ^{19}F OE DNP, using fluorobenzene as the solvent. The ^{19}F DNP field sweep profiles are shown in Figure 6. In direct analogy to the ^{1}H OE DNP case described earlier, decreases in efficiency are observed upon addition of a methyl group at position "1o". None of the radicals were effective for SE DNP, likely because this mechanism is dominated by non-methyl ^{1}H spins. The only fluorine atoms present in the radicals used for Figure 6 are part of CF_3 groups and would therefore be expected to have minimal SE activity.

4.5 | Theoretical Investigation of Methyl-Driven Overhauser DNP

We recently demonstrated the potential for using DFT calculations to gain mechanistic insights into methyl-driven Overhauser DNP effects [56]. DFT-calculated methyl rotation barriers and hyperfine coupling constants were found to be sufficient to rationalize the differences in OE DNP activity from different CF_3-functionalized Blatter radicals, despite these possibly containing significant errors. This precedent motivated this theoretical investigation to reveal why some of the 14 radicals studied here were found to be inactive.

15213765, 0, Downloaded from https://chemistry-europe.onlinelibrary.wiley.com/doi/10.1002/chem.71772 by Florida State University, Wiley Online Library on [02/11/2026]. See the Terms and Conditions (https://onlinelibrary.wiley.com/terms-and-conditions) on Wiley Online Library for rules of use; OA articles are governed by the applicable Creative Commons License

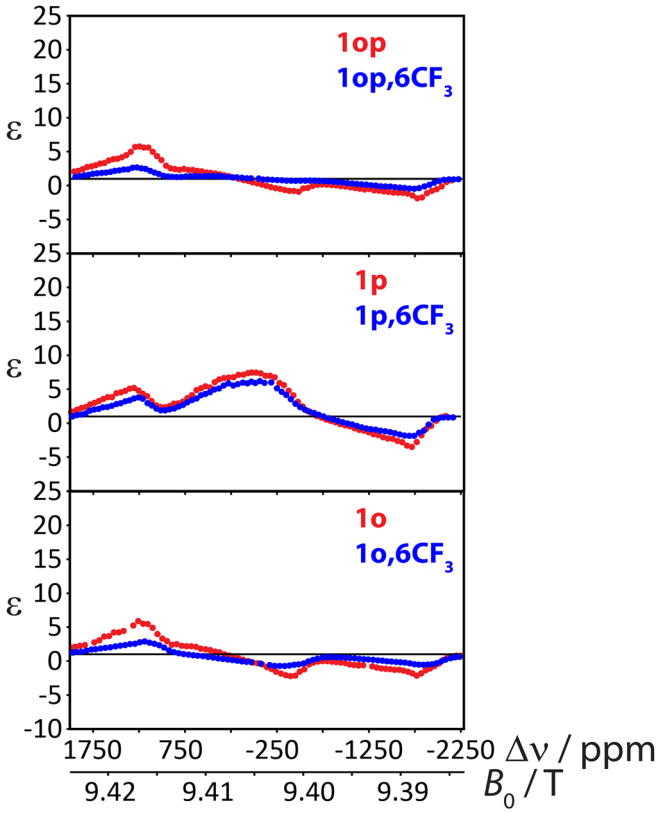


FIGURE 5 | ^{1}H DNP field sweep profiles measured for 6-CF_3-substituted Blatter radicals (blue). Each plot displays an overlay of the DNP field sweep profiles from this radical and the one lacking the additional CF_3 moiety (red). In all cases, both the OE and SE DNP enhancements are reduced by CF_3 addition.

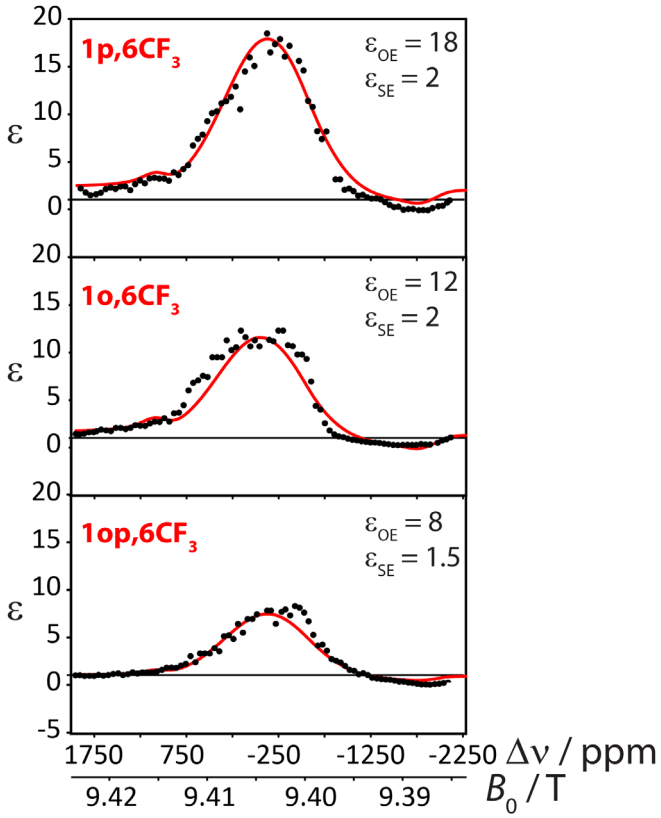


FIGURE 6 | ^{19}F DNP field sweep profiles measured for 6-CF_3-substituted Blatter radicals. Estimates of the DNP enhancements from the different mechanisms are given on the top right of each plot.

We performed potential energy surface scans as a function of the rotational phase of each methyl group in all 14 radicals. Additionally, we calculated the hyperfine coupling tensors at each dihedral angle increment to observe the modulation amplitude of the A_{iso} value. The results are shown in Figure 7, which groups each methyl group by its position on the benzotriazine core. The left panel shows the dependence of A_{iso} on the rotor phase, whereas the other two sets of panels plot the relative energy of the systems. Results are also tabulated in Table 2.

Focusing on the mono-functionalized radicals to start, which are shown in light blue in Figure 7, we can see that there is a strong modulation of the isotropic hyperfine coupling in five of the seven positions, with methyls at positions "1o" and "8" having limited hyperfine coupling. This agrees with the lack of OE seen experimentally in radicals **1o** and **8**. Additionally, we can note considerably larger rotation barriers for radicals **1o**, **5**, and **8**, above the optimal value of 1.7 kJ·mol^{-1}, suggesting that these radicals may have methyl rotations that are too slow to efficiently transfer hyperpolarization to protons by cross-relaxation.

Examining panel **1p** in Figure 7, the amplitude of the hyperfine coupling modulations is strongly affected by subsequent functionalizations that reduce the A_{iso} modulation amplitude, corresponding to the $\langle A_{iso}^2 \rangle$ term in Equation (5), and thus decreases OE activity. As seen in the experiment, the presence of a methyl group at the '1o' position induces the largest reduction. A second, albeit lower, drop is observed upon the addition of a CF_3 group at position number 6. Comparison of the plots of ΔE as a function of methyl phase reveals only minute changes as a function of secondary functionalization. The barrier heights are thus largely static quantities, and the differences in performance of a given methyl group from one radical to another are largely determined by the changes in hyperfine coupling strengths and not rotational rates.

Taken together, we used the calculated $\langle A_{iso}^2 \rangle$ and ΔE values in Table 2 to obtain DFT-calculated cross-relaxation rates for each methyl group and molecule. Importantly, these calculations successfully identified the radicals that were inactive for methyl-driven Overhauser DNP. Similarly, DFT calculations successfully identified the substitutions that lead to the greatest Overhauser enhancements. The correlation between the DFT-calculated cross-relaxation rates and the experimental DNP enhancements is plotted in Figure 8. Overall, we note a positive correlation between the two, which suggests that DFT is at least partly capturing the most relevant aspects of the mechanism. Deviation from linearity is nevertheless expected given the level of theory involved (DFT, lack of spin diffusion barrier consideration) and the importance of experimental variations resulting from partial radical oxidation.

Measurements were also performed at a magnetic field strength of 14.1 T for all the monomethylated radicals (see Table 2). For these, we again see a good correlation between experimental DNP

15213765, 0, Downloaded from https://chemistry-europe.onlinelibrary.wiley.com/doi/10.1002/chem.71772 by Florida State University, Wiley Online Library on [02/11/2026]. See the Terms and Conditions (https://onlinelibrary.wiley.com/terms-and-conditions) on Wiley Online Library for rules of use; OA articles are governed by the applicable Creative Commons License

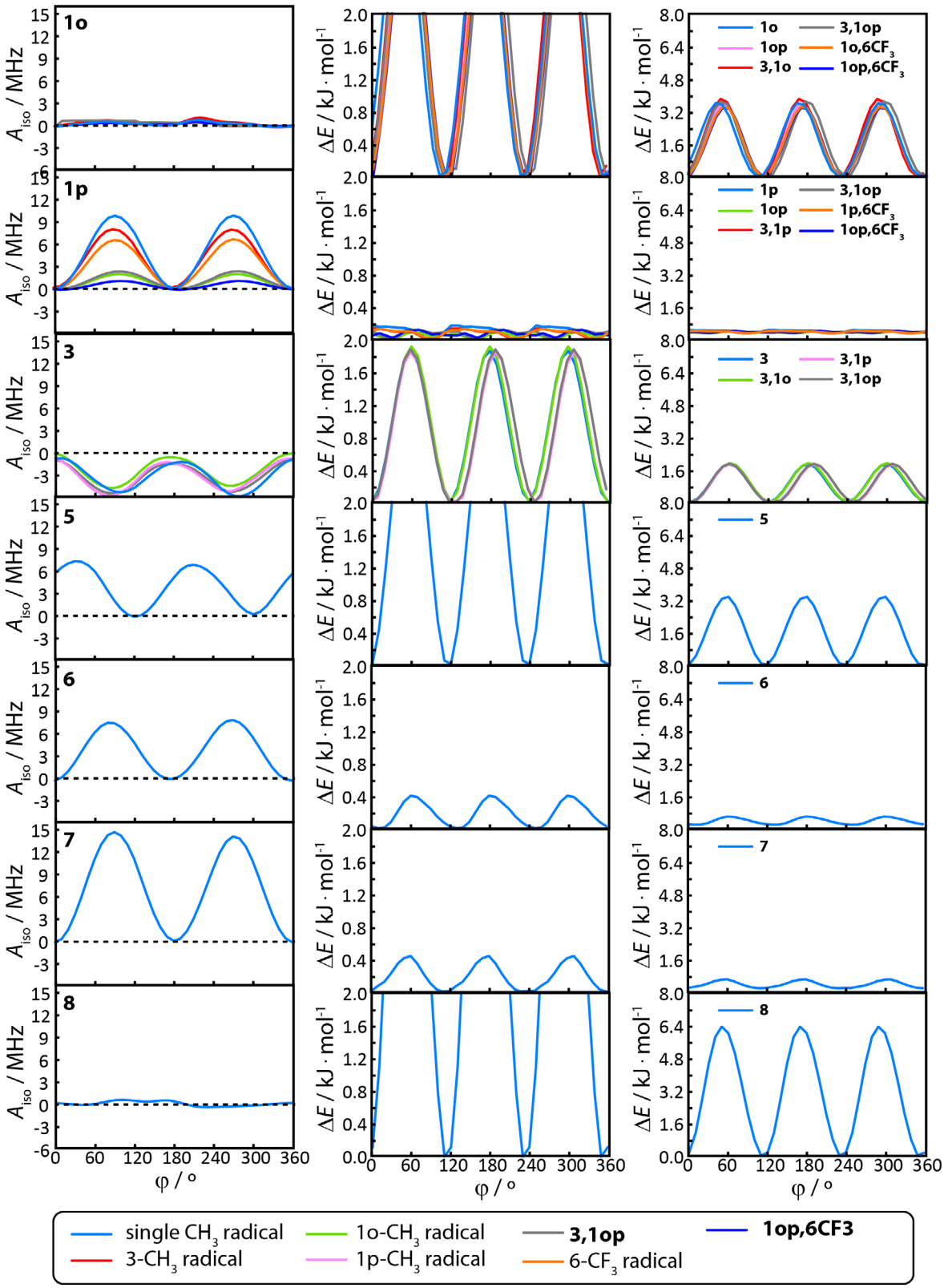


FIGURE 7 | DFT-calculated CH_3 rotor phase (φ) dependence of the ^1H isotropic hyperfine coupling constant (left) and the relative system energy (center and right). Each plot shows the corresponding dependence for a specific site on the Blatter core, as indicated on the plots on the left. Those calculated for poly-functionalized radicals are shown on the same plot with a different color according to the legend on the bottom. For example, the plot of A_{iso} versus φ for the methyl situated at the "1o" position in radical **1op** is shown in the top left plot in purple. The color assignments for each site are also clarified in the rightmost plots.

15213765, 0, Downloaded from https://chemistry-europe.onlinelibrary.wiley.com/doi/10.1002/chem.71772 by Florida State University, Wiley Online Library on [02/11/2026]. See the Terms and Conditions (https://onlinelibrary.wiley.com/terms-and-conditions) on Wiley Online Library for rules of use; OA articles are governed by the applicable Creative Commons License

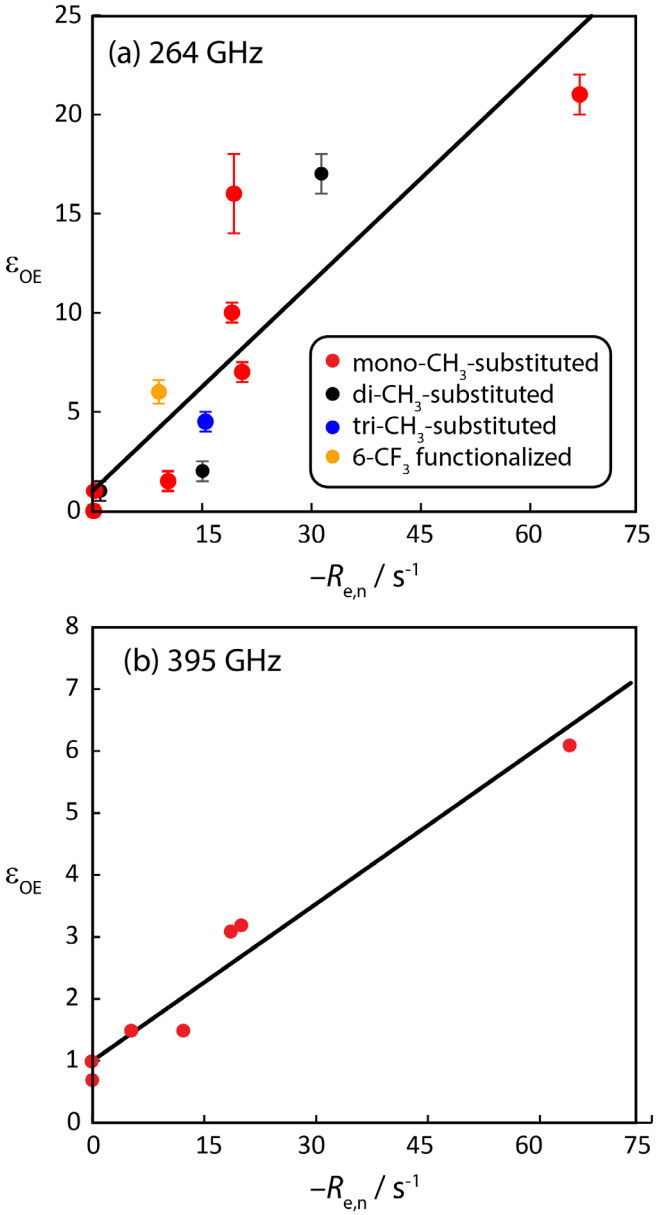


FIGURE 8 | Correlation between the experimental ^{1}H Overhauser effect DNP enhancements and the cross-relaxation rate calculated from CH_3 rotation using DFT calculations. Results from all radicals measured at 9.4 T are shown in (a), while results from the monomethylated radicals measured at 14.1 T are shown in (b). The fitted lines have intercepts at $\varepsilon_{OE} = 1$ and slopes of 1.051 ($R^2 = 0.77$; RMSE = 3.2) and 0.250 ($R^2 = 0.95$; RMSE = 0.38), respectively.

enhancements and DFT-calculated cross-relaxation rates (R^2 = 0.95), although the slope of the correlation is different, with the radicals yielding lower enhancements at the higher magnetic field strength. This may be due to the higher sample heating caused by the higher-frequency microwaves, or by incomplete saturation at the higher magnetic field, owing to the 50% larger *g* anisotropy at this field and lower microwave amplitude. The discrepancy may also be caused by the DFT calculations underestimating the rotation barriers, thus overestimating the methyl rotation frequency.

5 | Discussion

Within the Blatter-radical series examined here, these results allow us to identify structural features associated with high activity in methyl-driven Overhauser DNP (Figure 9). Even though the spin density function is distributed throughout the molecule by conjugation, we observed dramatic variations in Overhauser DNP performance. Of the seven singly-methylated radicals, only four were found to be active (**1p**, **3**, **6**, and **7**) whereas the other three (**1o**, **5**, **8**) were largely inactive with radical **5** showing evidence of a weak OE.

DFT calculations revealed that isotropic hyperfine coupling to the methyl protons in radicals **1o** and **8** was very weak (well below 1 MHz). Radical **5**, however, has a large computed mean isotropic hyperfine coupling constant ($\overline{A_{iso}}$) of 3.69 MHz and a high modulation amplitude ($\langle A_{iso}^2 \rangle$) of 12.70 MHz^2. The minimal Overhauser performance seen in this radical is instead explained by its high rotational barrier of 3.32 kJ·mol^{-1}, well above the optimal value of 1.70 kJ·mol^{-1}. Likewise, radicals **1o** and **8** also feature high ΔE values of 3.57 and 6.30 kJ·mol^{-1}, respectively. We hypothesize that these uniquely high barriers are caused by steric repulsion with the benzotriazine core, the nitrogen lone pair, and the N1-aryl moiety in the case of **1o**, **5**, and **8**, respectively. Importantly, none of the four radicals that displayed methyl-driven Overhauser activity had any sort of steric hindrance. It is thus likely that steric hindrance must be avoided for a methyl group to reach the 100s of GHz rotation frequencies required for cross-relaxation at high magnetic fields (Figure 9a).

We further observe that certain secondary functionalizations produce parasitic effects that reduce the overall Overhauser DNP performance. Specifically, addition of a methyl group at position "1o" led to a large reduction, or complete quenching, in the OE activity for all radicals, while the addition of a CF_3 moiety to a molecule led to a modest reduction in activity. These changes were not correlated to electron relaxation times but were well reproduced by DFT calculations. Given that we also found that rotational barriers were unaffected by such functionalization, the losses in performance must be attributed to changes in the spin density.

In the case of the 1o-methylated radicals, single-crystal x-ray diffraction structures suggest a likely explanation. Functionalization at this position leads to a large increase in the φ_{CNCC} dihedral angle values from 49 ± 8° to 73 ± 7° which is, for instance, expected to reduce the spin density at the "1p" position by a factor of four (Figure 9b). Indeed, while radical **1p** yielded a sizeable Overhauser DNP enhancement of 6.5, radical **1op** was completely inactive. Smaller inductive effects are seen in other radicals as well, suggesting that inductive effects are more widespread. For example, the Overhauser DNP enhancement is reduced from 10.0 in radical **3** to 2.0 in radical **3,1o**, which is associated with a reduction in the calculated proton hyperfine coupling constants to the methyl protons at position '3'. A similar effect is seen in a CF_3 site active in ^{19}F Overhauser DNP situated at position '6'. Specifically, ^{19}F OE enhancements were reduced from 18 in **1p,6CF$_3$** to 8 in **1op,6CF$_3$**.

Regarding the lower performance in ^{1}H OE DNP observed in CF_3-functionalized radicals, we initially suspected that the reduction

15213765, 0, Downloaded from https://chemistry-europe.onlinelibrary.wiley.com/doi/10.1002/chem.71772 by Florida State University, Wiley Online Library on [02/11/2026]. See the Terms and Conditions (https://onlinelibrary.wiley.com/terms-and-conditions) on Wiley Online Library for rules of use; OA articles are governed by the applicable Creative Commons License

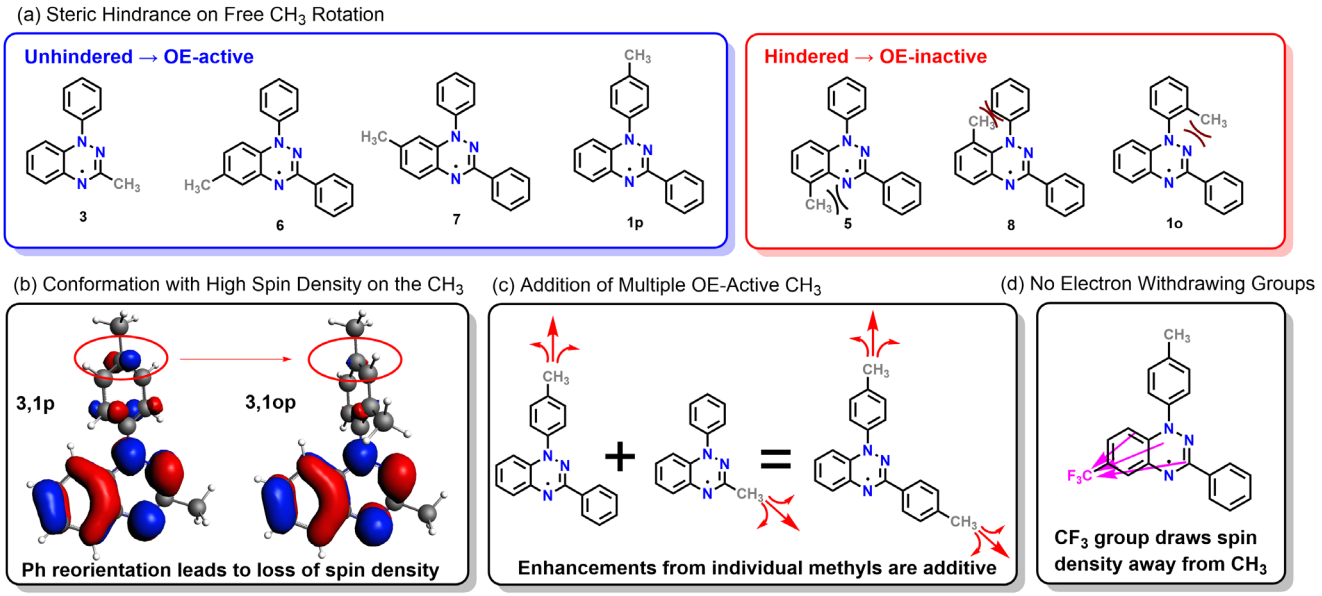


FIGURE 9 | Design principles for persistent free radical polarizing agents that will be active in methyl-driven Overhauser effect DNP: (a) the CH_3 group must be situated at a sp^2-hybridized site free from steric hindrance; (b) the conformation of the molecule must be such that significant spin density can exist at the methyl position; (c) the largest number of active CH_3 groups possible should be included; and (d) electron-withdrawing groups may draw spin density away from the methyl moiety, thus lowering A_{iso} and in turn the cross-relaxation rate.

was caused by a competition between ^{1}H and ^{19}F spins for the electron polarization; however, the reduction was well reproduced by DFT. These calculations showed that trifluoromethyl functionalization of the benzotriazine core instead draws electron density away from methyl moieties. For instance, a twofold reduction in hyperfine coupling is calculated when comparing radical **1p** to **1p,6CF$_3$** which in turn is correlated to a modest reduction in enhancement factor from 6.5 to 6.0. The fact that radical **1p,6CF$_3$** yielded both the largest ^{1}H and ^{19}F Overhauser DNP enhancements of the CF_3-functionalized radicals further cements the argument that the changes in performance are not the result of competition.

Not all functionalizations were parasitic. Of particular interest is the synthesis of radicals containing multiple methyl groups that are Overhauser-active given that cross-relaxation is expected to be additive for each proton involved. Of those studied here, only radical **3,1p** fell in this category. Monomethylated radicals **1p** and **3** yielded modest enhancements of 6.5 and 10.0, respectively, whereas radical **3,1p** yielded an Overhauser DNP enhancement of 17.0, roughly equal to the sum of the other two, as hypothesized. Assuming that *ortho*-methylations would sterically quench methyl-driven Overhauser DNP, it is likely that optimal performance in a Blatter system would be achieved in a trimethylated radical containing methyl moieties at positions "1p," "3," and either "6" or "7."

These observations suggest a set of design considerations for methyl-driven Overhauser DNP polarizing agents within the Blatter-radical scaffold, which can be assessed by inspection of a proposed chemical structure (Figure 9). Namely, it appears to be highly important that methyl groups are introduced in locations on a conjugated radical core with low steric hindrance to methyl rotation and that secondary functionalizations do not perturb the conjugation of the singly occupied molecular orbital. Ideally, as many OE-active methyl groups as possible should be included in the structure given that they are expected to behave largely independently of one another. Lastly, it also seems that electron-withdrawing groups may have a slight negative effect on methyl-driven Overhauser DNP (Figure 9d), although the added stability may enable the introduction of a greater number of methyl groups to the radical, leading to a greater overall performance [89].

6 | Conclusions

We studied the OE DNP efficiency of fourteen methyl-functionalized Blatter radicals to better understand the mechanism and derive design principles for efficient Blatter-type Overhauser DNP polarizing agents. Only radicals with methyl moieties sterically unhindered by a neighboring aryl group or lone pair were active in OE DNP. DFT calculations reveal that proximities which hinder methyl rotation limit cross-relaxation by slowing rotation well below the 100s of GHz required. Methyl substitution at two structurally decoupled positions produces a proportional increase in DNP efficiency, with both methyls acting independently. Other functionalizations, however, induce parasitic effects that reduce or completely quench OE DNP activity. Specifically, a methyl substituent at the *ortho* position of the N1-aryl moiety significantly alters the structural conformation, decoupling it from the SOMO and suppressing the OE of a methyl group at the *para* position. Addition of electron-withdrawing groups also reduces efficiency by withdrawing spin density from the Overhauser-active methyl group.

These observations highlight key design principles within this radical scaffold for improved polarizing agents: multiple methyl groups should be positioned at isolated locations on a conjugated

15213765, 0, Downloaded from https://chemistry-europe.onlinelibrary.wiley.com/doi/10.1002/chem.71772 by Florida State University, Wiley Online Library on [02/11/2026]. See the Terms and Conditions (https://onlinelibrary.wiley.com/terms-and-conditions) on Wiley Online Library for rules of use; OA articles are governed by the applicable Creative Commons License

radical with high π spin density. Electron-withdrawing groups should be avoided for optimal performance, although their effect can be partially offset by adding methyl substituents.

Author Contributions

Ananya Mukherji: investigation. **Emma A. Foley:** investigation. **Shubha S. Gunaga:** investigation; writing – review editing. **Thierry Dubroca:** investigation; writing – review editing. **Mukaila A. Ibrahim:** investigation. **Jin Seok-Yi:** investigation. **Nisreen Sharara:** investigation. **Syed Raza:** investigation. **Fadwat Bazzi:** investigation. **Simona Marincean:** investigation. **Dragos F. Flesariu:** investigation; writing – review editing. **Panayiotis A. Koutentis:** writing – review editing; conceptualization. **Frédéric Mentink-Vigier:** investigation; writing – review editing. **Takeshi Kobayashi:** conceptualization; investigation; writing – review editing; formal analysis; supervision. **Christos P. Constantinides:** investigation; writing – review editing; supervision; conceptualization; funding acquisition. **Frédéric A. Perras:** investigation; writing – review editing; supervision; conceptualization; formal analysis; funding acquisition.

Acknowledgments

This work was supported by the Department of Energy, Office of Science, Basic Energy Sciences through a Funding for Accelerated, Inclusive Research (FAIR) grant (Contract No. DE-SC0025694) at the University of Michigan-Dearborn (synthesis: AM, MAI, JSY, NS, SR, FB, SM, CPC) and Ames National Laboratory (NMR and theory: EAF, TK, FAP). EAF acknowledges the ISU-AMES Student-Centric Internships, Enabling Next-Generation Critical Energy Sciences (ISU-AMES SCIENCES) program. Ames National Laboratory is operated for the DOE by Iowa State University under Contract No. DE-AC02-07CH11358. DFF and PAK are grateful for funding from the Horizon Europe Framework Programme under the Marie Skłodowska-Curie Doctoral Networks (Grant Agreement 101119780; project duration: from Feb. 1, 2024, to Jan. 31, 2028). The National High Magnetic Field Laboratory (NHMFL) is funded by the National Science Foundation Division of Materials Research (DMR-2128556) and the State of Florida. NMR instrumentation used in this research was developed by the NIH National Resource for Advanced NMR Technology supported by RM1 GM148766. We acknowledge the use of the x-ray facility at the University of Michigan, Department of Chemistry. We thank Dr. Fengrui Qu for assistance with single-crystal data collection and analysis.

Conflicts of Interest

The authors declare no conflicts of interest.

Data Availability Statement

Additional crystallographic, EPR, and characterization data are made available as supporting information. Crystal structures may be obtained from the Cambridge Crystallographic Data Centre with the IDs: 2546239–2546244. Additional raw data are made available at 10.5281/zenodo.19923155. This includes all DFT input and output files, the DNP field sweep profiles, and the EPR relaxation data.

References

1. A. W. Overhauser, "Polarization of Nuclei in Metals," *Physical Review* 92 (1953): 411–415.

2. T. R. Carver and C. P. Slichter, "Polarization of Nuclear Spins in Metals," *Physical Review* 92 (1953): 212–213.

3. T. Maly, G. T. Debelouchina, V. S. Bajaj, et al., "Dynamic Nuclear Polarization at High Magnetic Fields," *Journal of Chemical Physics* 128 (2008): 052211.

4. M. Rosay, L. Tometich, S. Pawsey, et al., "Solid-State Dynamic Nuclear Polarization at 263 GHz: Spectrometer Design and Experimental Results," *Physical Chemistry Chemical Physics* 12 (2010): 5850–5860.

5. I. V. Sergeyev, F. Aussenac, A. Purea, et al., "Solid-State Dynamic Nuclear Polarization at 263 GHz," *Solid State Nuclear Magnetic Resonance* 100 (2019): 63–69.

6. M. C. D. Widanage, K. Singh, J. Li, et al., "Distinct Echinocandin Responses of *Candida albicans* and *Candida auris* Cell Walls Revealed by Solid-State NMR," *Nature Communications* 16 (2025): 6295.

7. W. Zhao, E. C. Thomas, D. Debnath, et al., "Enriched Molecular-Level View of Saline Wetland Soil Carbon by Sensitivity-Enhanced Solid-State NMR," *Journal of the American Chemical Society* 147 (2025): 519–531.

8. X. Kang, A. Kirui, M. C. D. Widanage, F. Mentink-Vigier, D. J. Cosgrove, and T. Wang, "Ligni-npolysaccharide interactions in plant secondary cell walls revealed by soli-dstate NMR," *Nature Communications* 10 (2019): 347.

9. F. A. Perras, H. Luo, X. Zhang, N. S. Mosier, M. Pruski, and M. M. Abu-Omar, "Atomic-Level Structure Characterization of Biomass Pre- and Post-Lignin Treatment by Dynamic Nuclear Polarization-Enhanced Solid-State NMR," *Journal of Physical Chemistry A* 121 (2017): 623–630.

10. T. Yagita, S. Paul, W. Papawassiliou, et al., "Atomic Structure of Phosphorylated Nanocellulose Revealed by Dynamic Nuclear Polarization-Enhanced Solid-State NMR," *Journal of the American Chemical Society* 148 (2026): 4237–4249.

11. A. Lesage, M. Lelli, D. Gajan, et al., "Surface Enhanced NMR Spectroscopy by Dynamic Nuclear Polarization," *Journal of the American Chemical Society* 132 (2010): 15459–15461.

12. L. Piveteau, T.-C. Ong, A. J. Rossini, L. Emsley, C. Copéret, and M. V. Kovalenko, "Structure of Colloidal Quantum Dots From Dynamic Nuclear Polarization Surface Enhanced NMR Spectroscopy," *Journal of the American Chemical Society* 137 (2015): 13964–13971.

13. F. A. Perras, A. L. Paterson, Z. H. Syed, et al., "Revealing the Configuration and Conformation of Surface Organometallic Catalysts With DNP-Enhanced NMR," *Journal of Physical Chemistry C* 125 (2021): 13433–13442.

14. R. W. Dorn, M. J. Ryan, T.-H. Kim, et al., "Identifying the Molecular Edge Termination of Exfoliated Hexagonal Boron Nitride Nanosheets With Solid-State NMR Spectroscopy and Plane-Wave DFT Calculations," *Chemistry of Materials* 32 (2020): 3109–3121.

15. P. Berruyer, M. Lelli, M. P. Conley, et al., "Three-Dimensional Structure Determination of Surface Sites," *Journal of the American Chemical Society* 139 (2017): 849–855.

16. B. J. Ryan, M. P. Hanrahan, Y. Wang, et al., "Silicene, Siloxene, or Silicane? Revealing the Structure and Optical Properties of Silicon Nanosheets Derived From Calcium Disilicide," *Chemistry of Materials* 32 (2020): 795–804.

17. T. Y. Zhao, E. P. Greenstein, I. L. Peczak, K. R. Poeppelmeier, and F. A. Perras, "Observing the Surface Termination of $LaScO_3$ Perovskite Using Solid-State Nuclear Magnetic Resonance," *Journal of the American Chemical Society* 146 (2024): 23487–23496.

18. A. Santhiran, F. Quinn, E. Gi, et al., "Probing the Surface Structure of Amine/Chloride-Passivated CdSe Nanocrystals Using Dynamic Nuclear Polarization-Enhanced ^{15}N, ^{35}Cl, ^{77}Se, and ^{113}Cd Solid-State NMR Spectroscopy," *Journal of the American Chemical Society* 148 (2026): 2563–2579.

19. S. Badoni, M. Terlecki, S. Carret, et al., "Atomic-Level Structure of the Organic-Inorganic Interface of Colloidal ZnO Nanoplatelets From Dynamic Nuclear Polarization-Enhanced NMR," *Journal of the American Chemical Society* 146 (2024): 27655–27667.

20. G. Menzildjian, J. Schlagnitweit, G. Casano, O. Ouari, D. Gajan, and A. Lesage, "Polarizing Agents for Efficient High Field DNP Solid-State NMR Spectroscopy Under Magic-Angle Spinning: From Design Principles to Formulation Strategies," *Chemical Science* 14 (2023): 6120–6148.

15213765, 0, Downloaded from https://chemistry-europe.onlinelibrary.wiley.com/doi/10.1002/chem.71772 by Florida State University, Wiley Online Library on [02/11/2026]. See the Terms and Conditions (https://onlinelibrary.wiley.com/terms-and-conditions) on Wiley Online Library for rules of use; OA articles are governed by the applicable Creative Commons License

21. F. Mentink-Vigier, I. Marin-Montesinos, A. P. Jagtap, et al., "Computationally Assisted Design of Polarizing Agents for Dynamic Nuclear Polarization Enhanced NMR: The AsymPol Family," *Journal of the American Chemical Society* 140 (2018): 11013–11019.

22. R. Wei, G. Casano, Y. Zhang, et al., "Systematic Evaluation of Polarizing Agents for Dynamic Nuclear Polarization Enhanced NMR," *Angewandte Chemie International Edition* 64 (2025): e202505944.

23. D. Leifert and A. Studer, "Organic Synthesis Using Nitroxides," *Chemical Reviews* 123 (2023): 10302–10380.

24. A. V. Yakimov, D. Mance, K. Searles, and C. Copéret, "A Formulation Protocol With Pyridine to Enable Dynamic Nuclear Polarization Surface-Enhanced NMR Spectroscopy on Reactive Surface Sites: Case Study With Olefin Polymerization and Metathesis Catalysts," *Journal of Physical Chemistry Letters* 11 (2020): 3401–3407.

25. H. Nagashima, J. Trébosc, Y. Kon, K. Sato, O. Lafon, and J.-P. Amoureux, "Observation of Low-γ Quadrupolar Nuclei by Surface-Enhanced NMR Spectroscopy," *Journal of the American Chemical Society* 142 (2020): 10659–10672.

26. W. R. Gunther, V. K. Michaelis, M. A. Caporini, R. G. Griffin, and Y. Román-Leshkov, "Dynamic Nuclear Polarization NMR Enables the Analysis of Sn-Beta Zeolite Prepared With Natural Abundance ^{119}Sn Precursors," *Journal of the American Chemical Society* 136 (2014): 6219–6222.

27. E. Pump, J. Viger-Gravel, E. Abou-Hamad, et al., "Reactive Surface Organometallic Complexes Observed Using Dynamic Nuclear Polarization Surface Enhanced NMR Spectroscopy," *Chemical Science* 8 (2017): 284–290.

28. E. Pump, A. Bendjeriou-Sedjerari, J. Viger-Gravel, et al., "Predicting the DNP-SENS Efficiency in Reactive Heterogeneous Catalysts From Hydrophilicity," *Chemical Science* 9 (2018): 4866–4872.

29. W.-C. Liao, T.-C. Ong, D. Gajan, et al., "Dendritic Polarizing Agents for DNP SENS," *Chemical Science* 8 (2016): 416–422.

30. I. Katz, A. Feintuch, R. Carmieli, et al., "Dynamic Nuclear Polarization Enhancement of 13C in Glucose Using Electrical Discharge Induced Radicals as Polarizing Agents," *Journal of Magnetic Resonance Open* 10–11 (2022): 100043.

31. S. L. Carnahan, A. Venkatesh, F. A. Perras, J. F. Wishart, and A. J. Rossini, "High-Field Magic Angle Spinning Dynamic Nuclear Polarization Using Radicals Created by γ-Irradiation," *Journal of Physical Chemistry Letters* 10 (2019): 4770–4776.

32. S. L. Carnahan, Y. Chen, J. F. Wishart, J. W. Lubach, and A. J. Rossini, "Magic Angle Spinning Dynamic Nuclear Polarization Solid-State NMR Spectroscopy of γ-Irradiated Molecular Organic Solids," *Solid State Nuclear Magnetic Resonance* 119 (2022): 101785.

33. S. L. Carnahan, K. Riemersma, I. Z. Hlova, et al., "Formation of Stable Radicals by Mechanochemistry and Their Application for Magic Angle Spinning Dynamic Nuclear Polarization Solid-State NMR Spectroscopy," *Journal of Physical Chemistry A* 128 (2024): 3635–3645.

34. O. Haze, B. Corzilius, A. A. Smith, R. G. Griffin, and T. M. Swager, "Water-Soluble Narrow-Line Radicals for Dynamic Nuclear Polarization," *Journal of the American Chemical Society* 134 (2012): 14287–14290.

35. K. R. Thurber, T.-N. Le, V. Changcoco, and D. J. R. Brook, "Verdazyl-Ribose: A New Radical for Solid-State Dynamic Nuclear Polarization at High Magnetic Field," *Journal of Magnetic Resonance* 289 (2018): 122–131.

36. T. Wolf, S. Kumar, H. Singh, et al., "Endogenous Dynamic Nuclear Polarization for Natural Abundance ^{17}O and Lithium NMR in the Bulk of Inorganic Solids," *Journal of the American Chemical Society* 141 (2019): 451–462.

37. F. A. Perras, D. F. Flesariu, S. A. Southern, et al., "Methyl-Driven Overhauser Dynamic Nuclear Polarization," *Journal of Physical Chemistry Letters* 13 (2022): 4000–4006.

38. Y. Rao, C. T. Palumbo, A. Venkatesh, et al., "Design Principles for the Development of Gd(III) Polarizing Agents for Magic Angle Spinning Dynamic Nuclear Polarization," *Journal of Physical Chemistry C* 126 (2022): 11310–11317.

39. I. B. Moroz, Y. Feldman, R. Carmieli, X. Liu, and M. Leskes, "Endogenous Metal-ion Dynamic Nuclear Polarization for NMR Signal Enhancement in Metal Organic Frameworks," *Chemical Science* 15 (2024): 336–348.

40. R. S. Palani, M. Mardini, Y. Quan, and R. G. Griffin, "Dynamic Nuclear Polarization With Trityl Radicals," *Journal of Magnetic Resonance* 349 (2023): 107411.

41. K.-N. Hu, C. Song, H.-H. Yu, T. M. Swager, and R. G. Griffin, "High-Frequency Dynamic Nuclear Polarization Using Biradicals," *Journal of Chemical Physics* 128 (2008): 052302.

42. K. R. Thurber and R. Tycko, "Theory for Cross Effect Dynamic Nuclear Polarization Under Magic-Angle Spinning in Solid State Nuclear Magnetic Resonance: The Importance of Level Crossings," *Journal of Chemical Physics* 137 (2012): 084508.

43. C. D. Jeffries, "Polarization of Nuclei by Resonance Saturation in Paramagnetic Crystals," *Physical Review* 106 (1957): 164–165.

44. F. A. Perras, F. Mentink-Vigier, and S. Pylaeva, "Perspectives on the Dynamic Nuclear Polarization Mechanisms of Monoradicals: Overhauser Effect or Thermal Mixing?," *Journal of Physical Chemistry Letters* 16 (2025): 3420–3432.

45. Z. Miao, F. J. Scott, J. van Tol, C. R. Bowers, A. S. Veige, and F. Mentink-Vigier, "Soliton Based Dynamic Nuclear Polarization: An Overhauser Effect in Cyclic Polyacetylene at High Field and Room Temperature," *Journal of Physical Chemistry Letters* 15 (2024): 3369–3375.

46. M. A. Hope, B. L. D. Rinkel, A. B. Gunnarsdóttir, et al., "Selective NMR Observation of the SEI–Metal Interface by Dynamic Nuclear Polarisation From Lithium Metal," *Nature Communications* 11 (2020): 2224.

47. J. van Bentum, B. van Meerten, M. Sharma, and A. Kentgens, "Perspectives on DNP-Enhanced NMR Spectroscopy in Solutions," *Journal of Magnetic Resonance* 264 (2016): 59–67.

48. G. Liu, M. Levien, N. Karschin, G. Parigi, C. Luchinat, and M. Bennati, "One-Thousand-Fold Enhancement of High Field Liquid Nuclear Magnetic Resonance Signals at Room Temperature," *Nature Chemistry* 9 (2017): 676–680.

49. T. V. Can, M. A. Caporini, F. Mentink-Vigier, et al., "Overhauser Effects in Insulating Solids," *Journal of Chemical Physics* 141 (2014): 064202.

50. S. Pylaeva, K. L. Ivanov, M. Baldus, D. Sebastiani, and H. Elgabarty, "Molecular Mechanism of Overhauser Dynamic Nuclear Polarization in Insulating Solids," *Journal of Physical Chemistry Letters* 8 (2017): 2137–2142.

51. S. Pylaeva, P. Marx, G. Singh, T. D. Kühne, M. Roemelt, and H. Elgabarty, "Organic Mixed-Valence Compounds and the Overhauser Effect in Insulating Solids," *Journal of Physical Chemistry A* 125 (2021): 867–874.

52. A. Gurinov, B. Sieland, A. Kuzhelev, et al., "Mixed-Valence Compounds as Polarizing Agents for Overhauser Dynamic Nuclear Polarization in Solids," *Angewandte Chemie International Edition* 60 (2021): 15371–15375.

53. L. Delage-Laurin, R. S. Palani, N. Golota, et al., "Overhauser Dynamic Nuclear Polarization With Selectively Deuterated BDPA Radicals," *Journal of the American Chemical Society* 143 (2021): 20281–20290.

54. T. Maly, D. Cui, R. G. Griffin, and A.-F. Miller, "^{1}H Dynamic Nuclear Polarization Based on an Endogenous Radical," *Journal of Physical Chemistry B* 116 (2012): 7055–7065.

55. F. A. Perras, Y. Matsuki, S. A. Southern, et al., "Mechanistic Origins of Methyl-Driven Overhauser DNP," *Journal of Chemical Physics* 158 (2023): 154201.

15213765, 0, Downloaded from https://chemistry-europe.onlinelibrary.wiley.com/doi/10.1002/chem.71772 by Florida State University, Wiley Online Library on [02/11/2026]. See the Terms and Conditions (https://onlinelibrary.wiley.com/terms-and-conditions) on Wiley Online Library for rules of use; OA articles are governed by the applicable Creative Commons License

56. S. A. Southern, G. A. Zissimou, D. F. Flesariu, et al., "In Silico Design of Methyl-Driven Overhauser Dynamic Nuclear Polarization Agents," *Journal of Physical Chemistry Letters* 16 (2025): 6219–6225.

57. S. R. Chaudhari, D. Wisser, A. C. Pinon, et al., "Dynamic Nuclear Polarization Efficiency Increased by Very Fast Magic Angle Spinning," *Journal of the American Chemical Society* 139 (2017): 10609–10612.

58. K.-N. Hu, H.-H. Yu, T. M. Swager, and R. G. Griffin, "Dynamic Nuclear Polarization With Biradicals," *Journal of the American Chemical Society* 126 (2004): 10844–10845.

59. C. Song, K.-N. Hu, C.-G. Joo, T. M. Swager, and R. G. Griffin, "TOTAPOL: A Biradical Polarizing Agent for Dynamic Nuclear Polarization Experiments in Aqueous Media," *Journal of the American Chemical Society* 128 (2006): 11385–11390.

60. Y. Matsuki, T. Maly, O. Ouari, et al., "Dynamic Nuclear Polarization With a Rigid Biradical," *Angewandte Chemie International Edition* 48 (2009): 4996–5000.

61. A. Zagdoun, G. Casano, O. Ouari, et al., "Large Molecular Weight Nitroxide Biradicals Providing Efficient Dynamic Nuclear Polarization at Temperatures up to 200 K," *Journal of the American Chemical Society* 135 (2013): 12790–12797.

62. A. Venkatesh, G. Casano, Y. Rao, et al., "Deuterated TEKPol Biradicals and the Spin-Diffusion Barrier in MAS DNP," *Angewandte Chemie International Edition* 62 (2023): e202304844.

63. G. Mathies, M. A. Caporini, V. K. Michaelis, et al., "Efficient Dynamic Nuclear Polarization at 800 MHz/527 GHz With Trityl-Nitroxide Biradicals," *Angewandte Chemie International Edition* 54 (2015): 11770–11774.

64. D. Wisser, G. Karthikeyan, A. Lund, et al., "BDPA-Nitroxide Biradicals Tailored for Efficient Dynamic Nuclear Polarization," *Journal of the American Chemical Society* 140 (2018): 13340–13349.

65. H. M. Blatter and H. Lukaszewski, "A New Stable Free Radical," *Tetrahedron Letters* 9 (1968): 2701–2705.

66. C. P. Constantinides, E. Obijalska, and P. Kaszynski, "Access to 1,4-Dihydrobenzo[e][1,2,4]triazin-4-yl Derivatives," *Organic Letters* 18 (2016): 916–919.

67. C. P. Constantinides, J.-S. Yi, H. Dakdouk, and S. Marincean, "Positional Methyl Effects in Benzo[e][1,2,4]triazines—Synthesis and Crystal Structure Analysis of 5-Methyl-3-phenylbenzo[e][1,2,4]triazine and Its Precursor, N′-(3-Methyl-2-nitrophenyl)benzohydrazide," *Crystals* 16 (2026): 206.

68. C. P. Constantinides, S. Raza, F. Bazzi, N. Sharara, and S. Marincean, "Synthesis and Crystal Structures of 6- and 8-Methyl-3-phenyl-benzo[*e*][1,2,4]triazines," *Acta Crystallographica Section E: Crystallographic Communications* 81 (2025): 699–705.

69. M. F. Reich, P. F. Fabio, V. J. Lee, N. A. Kuck, and R. T. Testa, "Pyrido[3,4-e]-1,2,4-triazines and Related Heterocycles as Potential Antifungal Agents," *Journal of Medicinal Chemistry* 32 (1989): 2474–2485.

70. W. Wu, S. Fan, T. Li, L. Fang, B. Chu, and J. Zhu, "Cobalt-Catalyzed, Directed Intermolecular C–H Bond Functionalization for Multiheteroatom Heterocycle Synthesis: The Case of Benzotriazine," *Organic Letters* 23 (2021): 5652–5657.

71. A. A. Berezin, G. Zissimou, C. P. Constantinides, Y. Beldjoudi, J. M. Rawson, and P. A. Koutentis, "Route to Benzo- and Pyrido-Fused 1,2,4-Triazinyl Radicals via N′-(Het)aryl-N′-[2-nitro(het)aryl]hydrazides," *Journal of Organic Chemistry* 79 (2014): 314–327.

72. P. A. Koutentis and D. Lo Re, "Catalytic Oxidation of N-Phenylamidrazones to 1,3-Diphenyl-1,4-dihydro-1,2,4-benzotriazin-4-yls: An Improved Synthesis of Blatter's Radical," *Synthesis* 2010 (2010): 2075–2079.

73. CrysAlisPro Software System, Rigaku Oxford Diffraction, 2025.

74. O. V. Dolomanov, L. J. Bourhis, R. J. Gildea, J. A. K. Howard, and H. Puschmann, "OLEX2: A Complete Structure Solution, Refinement and Analysis Program," *Journal of Applied Crystallography* 42 (2009): 339–341.

75. G. M. Sheldrick, "SHELXT-Integrated Space-Group and Crystal-Structure Determination," *Acta Crystallographica Section A: Foundations and Advances* 71 (2015): 3–8.

76. G. M. Sheldrick, "Crystal Structure Refinement With SHELXL," *Acta Crystallographica Section C: Structural Chemistry* 71 (2015): 3–8.

77. P. A. S. Cruickshank, D. R. Bolton, D. A. Robertson, R. I. Hunter, R. J. Wylde, and G. M. Smith, "A Kilowatt Pulsed 94 GHz Electron Paramagnetic Resonance Spectrometer With High Concentration Sensitivity, High Instantaneous Bandwidth, and Low Dead Time," *Review of Scientific Instruments* 80 (2009): 103102.

78. J. P. Perdew, K. Burke, and M. Ernzerhof, "Generalized Gradient Approximation Made Simple," *Physical Review Letters* 77 (1996): 3865–3868.

79. D. P. Chong, E. van Lenthe, S. van Gisbergen, and E. J. Baerends, "Even-Tempered Slater-Type Orbitals Revisited: From Hydrogen to Krypton," *Journal of Computational Chemistry* 25 (2004): 1030–1036.

80. G. te Velde, R. M. Bickelhaupt, E. J. Baerends, et al., "Chemistry With ADF," *Journal of Computational Chemistry* 22 (2001): 931–967.

81. J. Autschbach, S. Patchkovskii, and B. Pritchard, "Calculation of Hyperfine Tensors and Paramagnetic NMR Shifts Using the Relativistic Zeroth-Order Regular Approximation and Density Functional Theory," *Journal of Chemical Theory and Computation* 7 (2011): 2175–2188.

82. Y. Li, A. Equbal, T. Tabassum, and S. Han, "^{1}H Thermal Mixing Dynamic Nuclear Polarization With BDPA as Polarizing Agents," *Journal of Physical Chemistry Letters* 11 (2020): 9195–9202.

83. B. A. Rosin, V. Thalakottoor, M. Baudin, et al., "Quantitative Analysis of Cross-Talk in Partly Deuterated Samples of Nuclear Spins Hyperpolarized by Dynamic Nuclear Polarization (DNP) in the Thermal Mixing Regime," *Physical Chemistry Chemical Physics* 25 (2023): 15040–15051.

84. D. Guarin, S. Marhabaie, A. Rossi, et al., "Characterizing Thermal Mixing Dynamic Nuclear Polarization via Cross-Talk Between Spin Reservoirs," *Journal of Physical Chemistry Letters* 8 (2017): 5531–5536.

85. L. M. Epasto, T. Maimbourg, A. Rosso, and D. Kurzbach, "Unified Understanding of the Breakdown of Thermal Mixing Dynamic Nuclear Polarization: The Role of Temperature and Radical Concentration," *Journal of Magnetic Resonance* 362 (2024): 107670.

86. E. Ravera, C. Luchinat, and G. Parigi, "Basic Facts and Perspectives of Overhauser DNP NMR," *Journal of Magnetic Resonance* 264 (2016): 78–87.

87. M. Bennati, C. Luchinat, G. Parigi, and M.-T. Türke, "Water ^{1}H Relaxation Dispersion Analysis on a Nitroxide Radical Provides Information on the Maximal Signal Enhancement in Overhauser Dynamic Nuclear Polarization Experiments," *Physical Chemistry Chemical Physics* 12 (2010): 5902–5910.

88. F. Mentink-Vigier, Ü. Akbey, H. Oschkinat, S. Vega, and A. Feintuch, "Theoretical Aspects of Magic Angle Spinning—Dynamic Nuclear Polarization," *Journal of Magnetic Resonance* 258 (2015): 102–120.

89. C. P. Constantinides, P. A. Koutentis, H. Krassos, J. M. Rawson, and A. J. Tasiopoulos, "Characterization and Magnetic Properties of a "Super Stable" Radical 1,3-Diphenyl-7-trifluoromethyl-1,4-dihydro-1,2,4-benzotriazin-4-yl," *Journal of Organic Chemistry* 76 (2011): 2798–2806.

90. C. P. Constantinides, P. A. Koutentis, and J. M. Rawson, "Ferromagnetic Interactions in a 1D Alternating Linear Chain of π-Stacked 1,3-Diphenyl-7-(thien-2-yl)-1,4-dihydro-1,2,4-benzotriazin-4-yl Radicals," *Chemistry—A European Journal* 18 (2012): 7109–7116.

91. E. T. Broadhurst, C. J. G. Wilson, G. A. Zissimou, et al., "A First-Order Phase Transition in Blatter's Radical at High Pressure," *Acta Crystallographica Section B: Structural Science, Crystal Engineering and Materials* 78 (2022): 107–116.

92. D. Shimon, K. A. Cantwell, L. Joseph, et al., "Large Room Temperature Bulk DNP of ^{13}C via P1 Centers in Diamond," *Journal of Physical Chemistry C* 126 (2022): 17777–17787.

15213765, 0, Downloaded from https://chemistry-europe.onlinelibrary.wiley.com/doi/10.1002/chem.71772 by Florida State University, Wiley Online Library on [02/11/2026]. See the Terms and Conditions (https://onlinelibrary.wiley.com/terms-and-conditions) on Wiley Online Library for rules of use; OA articles are governed by the applicable Creative Commons License

93. D. A. O'Brien, D. R. Duling, and Y. C. Fann, *WinSim Public EPR Software Tools* (National Institute of Environmental Health Sciences, 2002).

94. F. A. Neugebauer and G. Rimmler, "ENDOR and Triple Resonance Studies of 1,4-Dihydro-1,2,4-benzotriazinyl Radicals and 1,4-Dihydro-1,2,4-Benzotriazine Radical Cations," *Magnetic Resonance in Chemistry* 26 (1988): 595–600.

Supporting Information

Additional supporting information can be found online in the Supporting Information section.

Crystallographic, EPR, and characterization data in addition to detailed synthesis procedures. Additional references cited within the Supporting Information [93, 94].

Supporting File 1: chem71772-sup-0001-SuppMat.docx

15213765, 0, Downloaded from https://chemistry-europe.onlinelibrary.wiley.com/doi/10.1002/chem.71772 by Florida State University, Wiley Online Library on [02/11/2026]. See the Terms and Conditions (https://onlinelibrary.wiley.com/terms-and-conditions) on Wiley Online Library for rules of use; OA articles are governed by the applicable Creative Commons License